Proceedings of ISFOG 2025
5TH INTERNATIONAL SYMPOSIUM ON
FRONTIERS IN OFFSHORE GEOTECHNICS
Nantes, France | June 9-13 2025

ISBN 978-2-85782-758-0

Offshore wind turbine foundation in China: Theory and Practice

L. Z. Wang*, Y. Hong*, Z. Guo, Y. Y. Gao, M. F. Huang, L. L. Wang, H. Y. Jiang
Zhejiang University, Hangzhou, China

R. Liu
Tianjin University, Tianjin, China

B. He
POWERCHINA HuaDong Engineering Corporation Limited, Hangzhou, China

Y. F. Lin
Shanghai Investigation, Design & Research Institute Co., Ltd., Shanghai, China

G. K. Yuan
China Energy Engineering Group Guangdong Electric Power Design Institute Co., Ltd., Guangzhou, China

X. X. Feng
Jiangsu Longyuan Zhenhua Marine Engineering Co., Ltd, Nantong, China

S.G. Wu
Institute of Deep-sea Science and Engineering, Chinese Academy of Sciences, Sanya, China

P. Yin
Qingdao Institute of Marine Geology, China Geological Survey, Qingdao, China

* *wanglz@zju.edu.cn, yi_hong@zju.edu.cn (corresponding author)*

ABSTRACT: With the rapid economic growth in China coastal area, the demand for offshore wind energy has been growing enormously. More challenges are imposed on the foundations of offshore wind turbines (OWTs) in China over those in Europe, due to harsher environmental loadings (e.g., typhoon) and complicated ground conditions (e.g., very soft clay). Under such severe natural conditions, the approaches of foundation design and installation originated from Europe become inadequate. This keynote paper highlights the recent progress made by the authors' interdisciplinary team in advancing foundation design theory and installation methods, facilitating the development of offshore wind energy in China waters. It comprises five main parts along with practical examples: (i) typhoon extreme wind; (ii) modelling soil behaviour; (iii) soil-pile interaction models; and (iv) multibody dynamics and software (v) innovative techniques for monopile installation. The concluding section summaries the key issues of these advances, while calling on interdisciplinary efforts for deep-water foundation.

Keywords: Offshore wind turbine; typhoon; soft soils; foundation design; pile installation

1 INTRODUCTION

The rapid economic growth in China coastal area and the urgent national goal of carbon reduction have led to surging demand for renewable energy. Although China has been the world's largest offshore wind power producer since 2021, its offshore techniques have relied heavily on international guidelines such as IEC (2009), DNV-ST-0437 (2021), and DNV-ST-0126 (2021), most of which are European-led based on experiences in the North Sea, where 80% of Europe's offshore turbines have been installed. Compared to North Sea, OWT foundations in China face harsher environmental loadings (e.g., typhoon) and more challenging ground conditions (e.g., very soft clay), with higher potential of dynamic failures. The ongoing trend toward larger turbines further intensifies these challenges (Figure 1). Under these scenarios, the European approaches of foundation design and installation are inadequate, hindering offshore wind farm development in China. By the end of 2023, China's installed capacity of offshore wind power reached 38 GW, accounting for 48% of the global total, see Figure 2(a). The authors' interdisciplinary team has participated in 76 offshore wind farms, as illustrated in Figure 2(b).

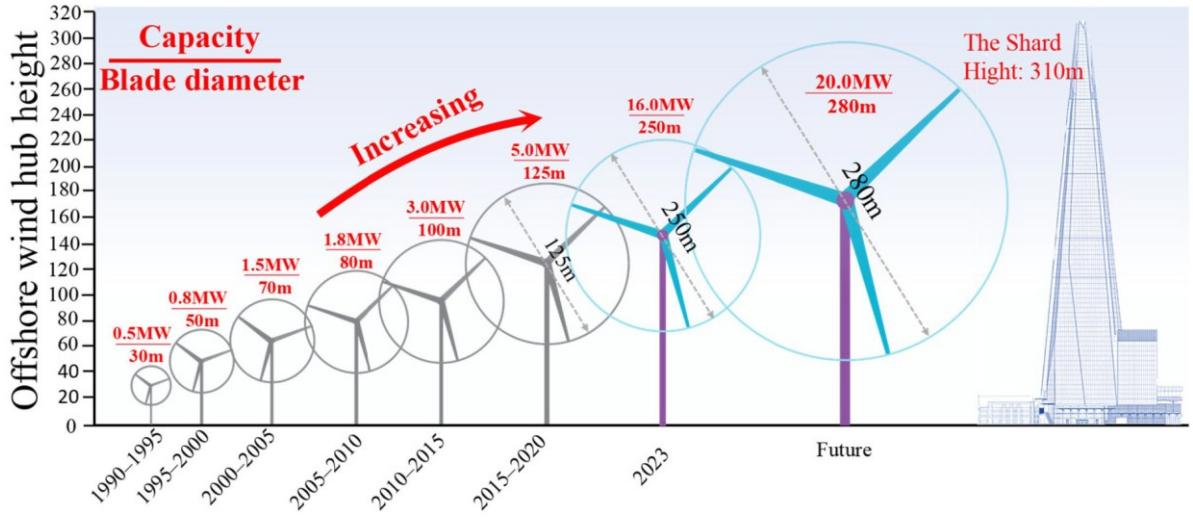

Figure 1. Development of large offshore wind turbines in China

Table 1 summarizes typical offshore wind foundation types deployed in four Chinese seas, including pile groups with elevated caps, monopiles, caissons, and pile-supported jackets (Figure 3). Monopiles dominate in most regions except in the South China Sea, where they are outnumbered by pile-supported jackets (Figure 3(d)). For limited space, this paper focuses on monopiles.

Typhoons have led to frequent failures of the foundations and structures of OWTs in China, which have drawn global attention. Recent revisions of DNV standard added additional requirements for typhoon conditions regarding mechanical response, electricity, safety and control systems, etc.

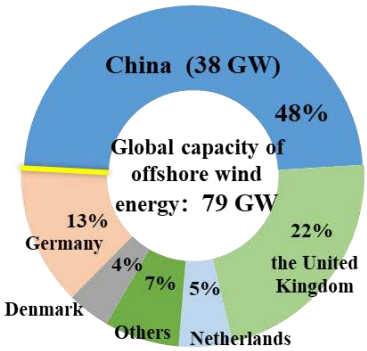

(a)

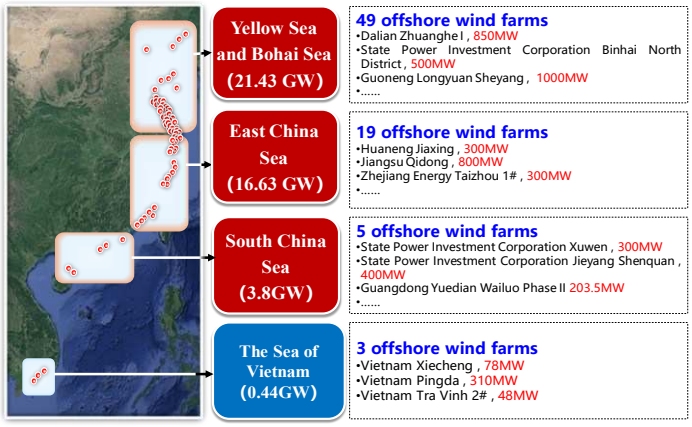

(b)

Figure 2. Offshore Wind Power Projects in China and Vietnam: A Summary of Team-Participated Projects

However, critical gaps remain, such as the typhoon-scale characteristics of wind and waves, load calculation methods, failure mechanisms and design approaches for foundations with varying rigidities in soft ground. Regarding design software, there is a lack of coupled aero-hydro-servo-elastic software with adequate considerations of typhoons and soil-pile interactions, which are vital for structural failure analysis and OWT foundation design in typhoon-prone area.

In the context of installation, deploying OWT foundations in China faces significant challenges due to the increasing pile dimension and weight. One major difficulty is the installation of thousand-ton pile foundations in ultra-soft seabed, where verticality control is critical.

Table 1. Typical types and numbers of offshore wind

	Monopile	Pile group with elevated cap	Suction bucket	Jacket pile foundation
Bohai	430	43	32	16
Yellow Sea	3054	124	50	117
East China Sea	473	656	2	0
South China Sea	780	0	6	435

This keynote paper presents recent advancements in developing foundation design theory and installation techniques customized to the harsh environments of China waters. It covers five key sections, supported by case studies: (i) typhoon extreme wind; (ii) modelling soil behaviour; (iii) soil-pile interaction models; and (iv) multibody dynamics and software; (v) innovative techniques for monopile installation. It concludes with the key findings and explores potential foundation innovations for deep-water.

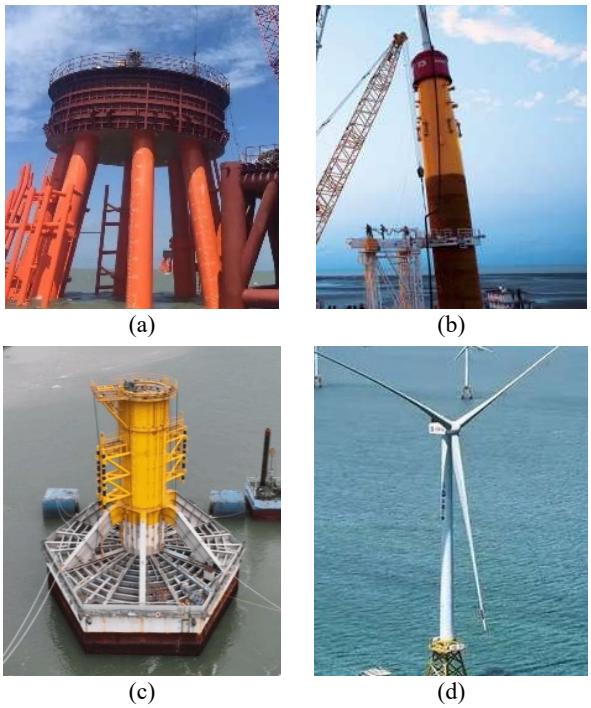

(a) (b) (c) (d)

Figure 3. Typical offshore wind foundation types in China: (a) pile group with elevated cap, (b) monopile, (c) monopod with large diameter and shallow embedment, (d) jacket pile foundation

2 TYPHOON EXTREME WIND

Typhoon is classified as a specific type of tropical cyclones (TCs) characterized by maximum sustained surface winds reaching or exceeding 32.7 m/s in 2-minute average. Southeast China is particularly vulnerable to the hazards associated with typhoons. Notably, Super-Typhoon Lekima, which made landfall in eastern China in 2019 with maximum 2-minute sustained winds reaching 52 m/s, resulted in direct economic losses of 53.72 billion Chinese yuan and claimed 56 lives. Given the increasing typhoon hazard risk amidst climate change, it is imperative to develop an efficient and effective TC model capable of accurately capturing typhoon characteristics.

Due to strongly heterogeneous characteristics of the historical TC tracks in the western North Pacific Ocean (WNP), cluster analysis has been proposed to explore the distinguished typhoon statistical characteristics of different zones of the WNP basin (Camargo, 2007; Mei, 2016). Since each cluster of historical TC tracks has a unique geographic feature, it is more efficient to establish a machine learning based TC model for each cluster category than for a whole basin.

The Random Forest (RF) algorithm is employed in this study to build the new TC models to replace the original Vickery linear regression model (Vickery et al., 2000) in the full track simulation framework. Random forest is an ensemble machine learning method with Classification and Regression Trees (CARTs) (Breiman, 2001).

The RF-based TC movement model can be expressed as follows:

$$\begin{cases} \Psi_{i+1} = RF_{\Psi}(\Psi_i, \lambda_i, \Psi_{i-1}, \lambda_{i-1}, \Psi_{i-2}, \lambda_{i-2}, \\ \qquad \Psi_{i-3}, \lambda_{i-3}) + \varepsilon_{\Psi} \\ \lambda_{i+1} = RF_{\lambda}(\Psi_i, \lambda_i, \Psi_{i-1}, \lambda_{i-1}, \Psi_{i-2}, \lambda_{i-2}, \\ \qquad \Psi_{i-3}, \lambda_{i-3}) + \varepsilon_{\lambda} \end{cases} \quad (1)$$

where RF_{Ψ} and RF_{λ} denote the RF-based TC movement models to predict the latitude Ψ and longitude λ of a moving TC center at the next time step of $i+1$; the last four steps, i.e., i, i-1, i-2 and i-3, are chosen as the main predictors of TC movement models; ε_{Ψ} and ε_{λ} are the randomly sampled error terms.

To validate the RF-based TC full track simulation method (Huang et al., 2022a), a series of tropical cyclone paths and intensity samples were generated. The key statistical parameter of the simulated tropical cyclones, i.e., annual occurrence of TC, was then calculated and compared to historical data for 25 selected sites along the coastline of China. The comparison results with the historical tropical cyclone statistics are shown in Figure 4. It can be seen that the annual occurrence of the simulated tropical cyclones for 25 coastal sites align well with the corresponding parameters of the historical tropical cyclones. The correlation coefficient R values are above 0.99, verifying the effectiveness of the RF-based TC full track simulation model.

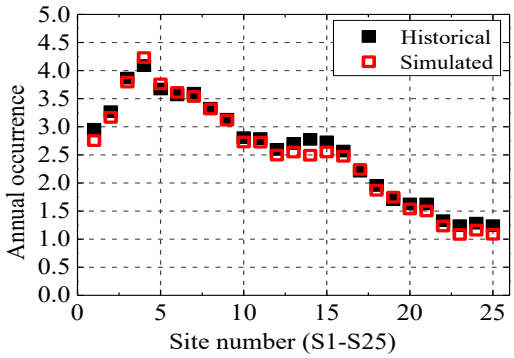

Figure 4. Comparison of annual occurrence of TC from simulation and historical dataset for 25 selected sites along the coastline of China

In the context of future global warming, a case under SSP5-8.5 scenario from the CMIP6 is studied with trained RF typhoon models, to predict the design wind speeds of offshore area of China at the end of the century (Huang et al., 2022b). Figure 5 presents the 100-year return period typhoon design wind speeds (mean wind speed averaged in two minutes) in the south-eastern coastal seas of China. In the future climate conditions, the extreme wind speeds are highest in the coastal seas of Taiwan Province, Zhejiang Province and Guangdong Province, with the extreme wind speed in the eastern coastal seas of Taiwan approaching 70 m/s.

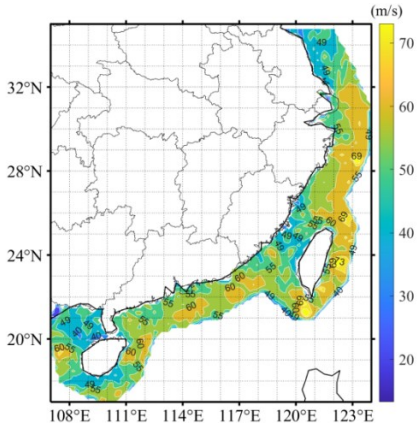

Figure 5. Typhoon wind speed distribution of 100-year return periods under SSP5-8.5 scenario in the late of 21st century

3 MODELLING SOIL BEHAVIOR

3.1 Offshore Geotechnical Site Investigation and Testing

A series of jack-up platforms for different water depths (15 m, 35 m, 55 m and 75 m) has been developed by Huadong Engineering Corporation limited (HDEC) in China. These platforms can perform intelligent drilling and sampling, in-situ testing, and geotechnical lab testing. Among others, 'HDEC 308' is the most advanced jack-up platform in China for offshore wind farm geotechnical investigation (Figure 6), with the longest pile leg length of 100 m, the largest deck area of 2200 m^2 and the highest wind withstanding level of 16. In addition, HDEC is equipped with advanced marine drilling and sampling system (Figure 7(a)), which can ensure high-quality sampling under condition of 80 m water depth and 2.5 m/s current velocity. Besides, seabed CPTU (Figure 7(b)) and downhole CPTU (Figure 7(c)) have been incorporated in site investigation for testing in deeper water and larger penetration depths.

Platform for 75 m water depth

Figure 6. Jack-up marine survey platforms

a) Top drive drilling system

b) Seabed CPTU

c) Downhole CPTU

Figure 7. Advanced marine drilling and in-situ testing devices

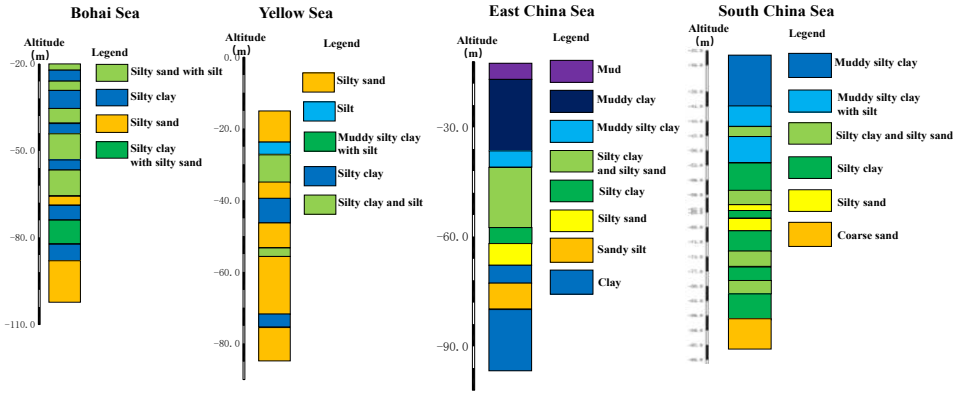

Figure 8. Typical geological strata in major sea areas of China（Qin et al., 2020）

Above equipment and technologies have been applied in various seas across China, performing high-quality and efficient investigations under different geotechnical conditions. Typical geological strata in China's four major seas (Qin et al., 2020) are shown in Figure 8.

3.2 Marine Clay Thermal-visco-elasto-plasticity

Natural clay usually exhibits significant anisotropy, with its microscopic fabric alignment induced by deposition and stress history leading to inclined yield surfaces and anisotropy in undrained shear strength (Leroueil and Marques 1996; Leroueil, 2001). The temperature discrepancy between in-situ seabed (0-4 ℃) and laboratory conditions (20 ± 2 ℃) implies that the undrained shear strength obtained in laboratory should be carefully corrected. Yield and shear strengths demonstrate strain-rate dependency, showing around 10% enhancement per order-of-magnitude strain rate increase (Leroueil, 1997). Under cyclic loading, stiffness degradation, plastic strain accumulation, and pore pressure redistribution occur, with hysteresis loops governed by loading characteristics. Special attention should be paid to cyclic weakening effects on seabed foundation stability. There are mainly two theories for soil plasticity modelling, including multiple surfaces and boundary surface (Dafalias, 1986; Asaoka, 2002; Liu et al., 2019), which have experienced mutually enhancement over the past two decades.

3.2.1 Yield surface and anisotropic undrained shear strength of natural marine clay

Nineteen different stress probe tests and four undrained triaxial tests on K_0-consolidated Wenzhou clay are analysed, and the yield surface as well as the plastic flow rule beyond yielding also studied (Wang and Shen, 2008). The initial yield surface of natural marine clay can be described by an inclined ellipse on the p'-q plane based on the yield function proposed by Wheeler et al. (2003), and the normality law is verified for describing the flow behaviour (Figure 9).

$$f = \frac{M^2 - \alpha^2 + (\eta - \alpha)^2}{M^2 - \alpha^2} p' - p_c' = 0 \qquad (2)$$

where α defines the orientation of the inclined ellipses, which represents the effects of plastic anisotropy. p_c' represent the size of the yield surface. η is stress ratio. M is the critical state stress ratio.

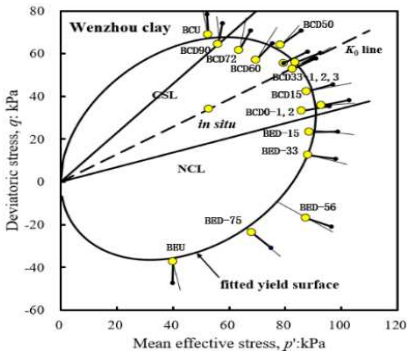

Figure 9. Yield surface and plastic flow direction of Wenzhou clay

On the basis of the critical state soil mechanics and the inclined ellipse yield surface, theoretical formulas of the undrained strength under K_0 compression and extension stress condition were derived (Wang et al., 2008):

$$\frac{s_u}{\sigma_{v0}'} = \frac{M}{2} \cdot \frac{1 + 2K_0}{3} \cdot \left(\frac{M \pm \alpha_0}{2M}\right)^{\Lambda} \left(\frac{M^2 + \eta_{K_{0nc}}^2 - 2\alpha_0 \eta_{K_{0nc}}}{M^2 - {\alpha_0}^2}\right)^{\Lambda} n^{\Lambda} \qquad (3)$$

where $\alpha_0 = \frac{\left(\eta_{K_{0nc}}^2 + 3\eta_{K_{0nc}} - M^2\right)}{3}$ is the inital value of iniclination of yield surface and $\eta_{K_{0nc}}$ represents the stress ratio of K_0-consolidated state. $\Lambda = 1 - \frac{\kappa}{\lambda}$ is the compression parameter. λ and κ denote the slopes of normal consolidation line (NCL) and elastic swelling line in $v - lnp'$ plane, respectively.

The measured and predicted s_u of three natural clay (i.e. Ariake clay, Weald clay and Mito clay) are

compared, as shown in Figure 10. The comparison results proved that Eq. (3) can reasonably capture the undrained shear strength of K_0 consolidated clay with different OCR values under both triaxial compression and extension conditions.

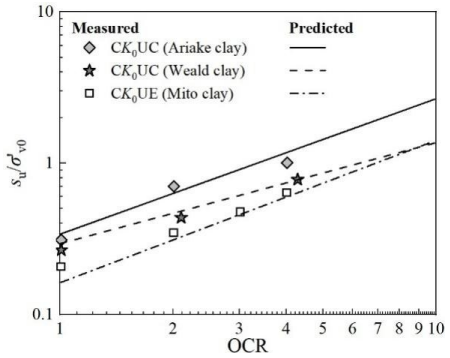

Figure 10. Comparison between the measured and predicted undrained shear strength of K0-consolidated clay

3.2.2 Temperature-dependent undrained shear strength

Building upon the anisotropic constitutive framework, a temperature-dependent model was developed through explicit incorporation of the thermomechanical coupling between preconsolidation pressure and thermal history. The relationship between preconsolidation pressure and temperature can be fitted by the following equation (Wang et al., 2016; Wang et al., 2020b):

$$p_c^{'} = p_{c0}^{'} \cdot exp\left(\frac{\varepsilon_v^p}{\frac{(\lambda-\kappa)}{v_i}}\right)\left(\frac{T_0}{T}\right)^{\theta} \tag{4}$$

where $p_{c0}^{'}$ is the initial preconsolidation pressure at reference temperature T_0. θ is a model parameter reflecting the temperature effect on the preconsolidation stress, and could be dertermined through the linearly correlation between the plasticity index I_P, as shown in Figure 11:

$$\theta = 0.1120 + 0.0012 I_P \tag{5}$$

A simplified equation for temperature-dependent undrained shear strength after drained heating is derived as:

$$\frac{s_u}{\sigma_{v0}^{'}} = \frac{M}{2}\frac{1+2K_0}{3} \cdot \left(\frac{M \pm \alpha_0}{2M}\right)^{\Lambda} \cdot n^{\Lambda} \cdot \left(\frac{T}{T_0}\right)^{\theta\Lambda} \tag{6}$$

A case study shows that laboratory triaxial undrained tests, which follows drained heating consolidation at 20 ℃, could induce 17% increase of s_u for samples from the deep waters (at 4 ℃) (Wang et al., 2016).

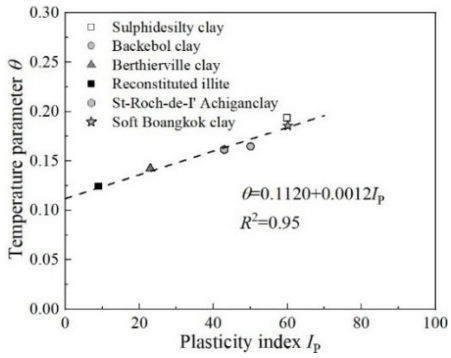

Figure 11. Correlation between the temperature related parameter and plasticity index

3.2.3 Strain-rate dependent preconsolidation pressure and undrained shear strength

The viscous behavior of soft soils is evident in creep and the types of strain-rate dependent phenomena. The undrained shear strength may increase by around 10% for a tenfold increase in strain rates. An anisotropic elastic-viscoplastic constitutive model was developed to simulate the strain-rate dependent behavior of K_0-consolidated soft clays. The constitutive equations are derived on the basis of the overstress concept, assuming inclined ellipses as contours of the viscoplastic scalar multiplier ϕ (Wang et al., 2012).

By analyzing the deformations in one-dimensional ($1D$) creep compression (Wang et al., 2012), the functional form of ϕ can be derived by:

$$\phi = \frac{\psi}{v_i t_0}\left(\frac{p_c'}{p_{c0}'}\right)^{\frac{\lambda-\kappa}{\psi}} exp\left(\frac{-\varepsilon_v^{vp}}{\frac{\psi}{v_i}}\right)\left(\frac{M^2-\alpha_0^2}{M^2-\eta_{K_{0nc}}^2}\right) \tag{7}$$

where $\psi = \frac{C_\alpha}{ln\,10}$ denotes the coefficient of secondary compression. $t_0 = 24h$ is the absolute time of the NCL. v_i denote the initial value of specific volume before shearing. ε_v^{vp} is the visco-plastic volumetric strain.

The analytical formulations of strain-rate dependent preconsolidation pressure and undrained shear strength are derived as:

$$\frac{\sigma_p^{'}}{\sigma_{p,\ 24h}^{'}} = \left(\frac{\dot{\varepsilon}_z}{\frac{\psi}{v_i t_0}}\right)^{(\psi/\lambda)/\Lambda} \tag{8}$$

$$\frac{s_u}{\sigma_{v0}^{'}} = \frac{M}{2}\cdot\frac{1+2K_0}{3} \cdot \left(\frac{M \pm \alpha_0}{2M}\right)^{\Lambda}\left(\frac{\dot{\varepsilon}_a}{\psi/v_i t_0}\frac{M^2-\eta_{K_{0nc}}^2}{2(M \mp \alpha_0)}\right)^{\psi/\lambda} n^{\Lambda} \tag{9}$$

where $\sigma'_{p,\ 24h}$ is the preconsolidation pressure measured from the standard 24-h oedometer test. n is the yield stress ratio.

Figure 12 shows the results of rate dependency of pre-consolidation pressures for 12 natural marine clays from the Champlain sea area in Eastern Canada. The proposed model can adequately describe the relationship of pre-consolidation pressure versus the axial strain rate, and most test data are in a narrow range of ± 7 % from the predicted curve.

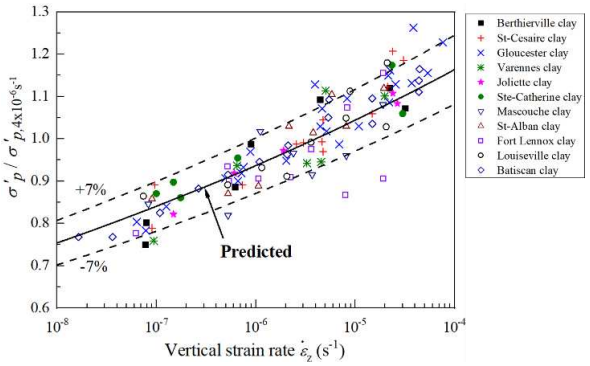

Figure 12. Measured and predicted preconsolidation pressure of Champlain sea clay at various strain rates

In order to verify the predictive capability of the Eq. (9), the undrained shear strength of a total of 26 clays under different shear strain rates were collected, as shown in Figure 13. It is revealed that Eq. (9) can well capture the increase trend of undrained shear strength with axial strain-rate.

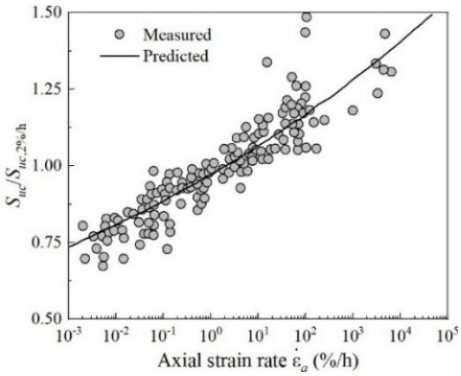

Figure 13. Measured and predicted undrained shear strength of different soils at different strain rates

3.2.4 Modelling cyclic behaviour: an equivalent creep simplification approach

In addition, the accumulative behaviour under undrained cyclic loading can be evaluated through combining a pseudo-static method of equivalent undrained creep with the above models. To theoretically simulate the accumulative behavior of clayey samples, the real undrained cyclic loading process is equivalent to a static undrained creep with a load increment $\Delta q = q_{\mathrm{cyc}}$, and the loading duration t is chosen as a basic modeling variable (Li et al., 2011).

$$\dot{\varepsilon}_{vn}^{\mathrm{vp}} = \frac{\psi}{v_i t} = \frac{\psi}{v_i t_0}\left(\frac{\sigma_v'}{\bar{\sigma}_v'}\right)^{\frac{(\lambda-\kappa)}{\psi}} \tag{10}$$

However, this simplification results in a shorter predicted rupture lifetime compared to experimental observations, as the soil experiences the peak deviator stress q_{cyc} for only a brief interval during each cycle.

To improve the validity and precision of the prediction, the coefficient of secondary compression, which is a key parameter in controlling the viscous behaviour of soils, was adjusted by the back-analysis method. The equivalent coefficient of secondary compression $\bar{C}_\alpha$ is proposed through the back analysis method and is linearly related to cyclic stress ratio $\frac{q_{\mathrm{cyc}}}{p_0'}$:

$$\frac{\bar{C}_\alpha}{C_\alpha} = A\left(\frac{q_{\mathrm{cyc}}}{p_0'}\right) + 1 \tag{11}$$

By using the pseudo-static method of equivalent creep and the proposed anisotropic TEVP model, the development of shear strain amplitudes and excess pore pressure of natural Wenzhou clay are generally well predicted, as illustrated in Figure 14.

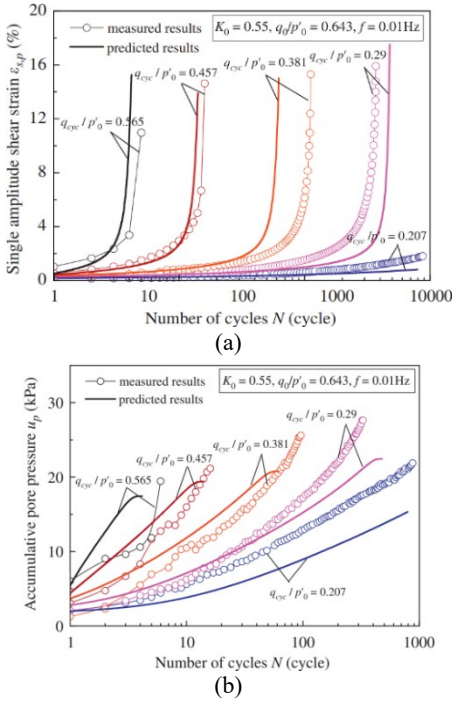

Figure 14. Comparison between measured and predicted accumulative behavior of natural Wenzhou clay (f=0.01 Hz): (a) shear strain, (b) pore pressure.

3.3 Sand Plasticity with Fabric Anisotropy

Wave induced liquefaction is a classic topic in offshore geotechnical community (Ishihara and

Towhata, 1983), but principal stress rotation does not produce residual pore pressure in the view of isotropic material plasticity. Marine sedimentation induces preferential orientation of sand particles, forming anisotropic fabric structures through hydrodynamic sorting and gravitational compaction. Such inherent fabric anisotropy fundamentally governs the stress-strain hysteresis observed in marine sands, requiring explicit representation of fabric tensors in anisotropic constitutive models. This can be achieved by introducing an anisotropic state parameter ζ (Li and Dafalias, 2012):

$$\zeta = e - e_c(p') - e_A(A-1) \tag{12}$$

where e_A is a material constant and $A = \boldsymbol{F} : \frac{\boldsymbol{R}^*}{\|\boldsymbol{R}^*\|}$ is the anisotropic variable expressed as the joint invariant between the fabric tensor $\boldsymbol{F}$ and the flow direction tensor $\frac{\boldsymbol{R}^*}{\|\boldsymbol{R}^*\|}$.

Using ζ, Hong et al. (2024) proposed a new dilatancy function to consider the effect of fabric on dilation:

$$D = \{A_0 g(\theta)^{-n_g}(1 + \langle \boldsymbol{z} : \boldsymbol{n} \rangle)(\boldsymbol{\alpha}_\theta^D - \boldsymbol{\alpha}) : \boldsymbol{n}\} \underbrace{exp[k_1(1-A)]}_{fabric\ dependent} \tag{13}$$

where n_g and k_1 are two material constants. The term $exp[k_1(1-A)]$ was introduced to describe fabric-related dilation based on experimental observations.

For the modelling of cyclic loading, the high-cycle strain accumulation and liquefaction of sands are usually described using the bounding surface plasticity enriched with a memory surface (Figure 15). The dependency of these surfaces on fabric anisotropy were formulated by Hong et al. (2024).

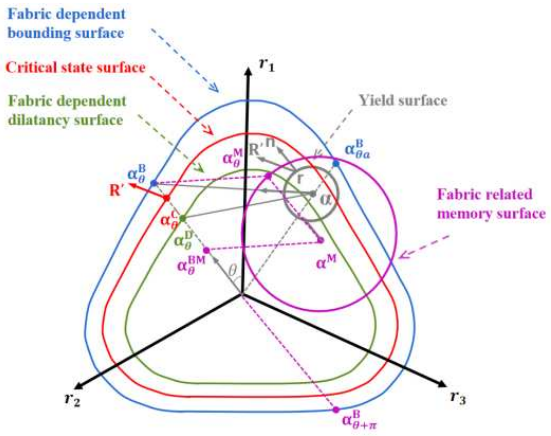

Figure 15. Schematic illustration of the model surfaces and mapping rules on the deviatoric stress ratio-plane.

A unified approach to simulate anisotropic drained and undrained cyclic behavior considering fabric anisotropy is established by incorporating the memory-to-yield distance $b^{\mathrm{M}} = (\boldsymbol{\alpha}^M - \boldsymbol{\alpha}) : \mathbf{n}$ into the plastic modulus K_p through the hardening coefficient h:

$$K_p = \left(\frac{2}{3}\right) p' h(\boldsymbol{\alpha}_\theta^B - \boldsymbol{\alpha}) : \boldsymbol{n} \tag{14}$$

where h captures the fabric effect as detailed in Papadimitriou et al. (2019) and Yang et al. (2022). A new fabric-related anisotropic hardening rule is also proposed, incorporating fabric anisotropy and its evolution into the expansion rate of the memory surface.

The performance of the proposed model in simulating anisotropic high-cycle behavior is validated via several sets of representative experiments, including a large-strain drained cyclic test with up to 10^4 cycles (Wichtmann, 2005), anisotropic cyclic drainage tests with different fabric bedding plane angles (Hong et al., 2024), and undrained cyclic tests. Figure 16 examplifies one unique feature of the proposed model, which manages to capture the transition from cyclic shakedown to ratcheting for sands with the same voild ratio and mean effective stress but different fabric orentations.

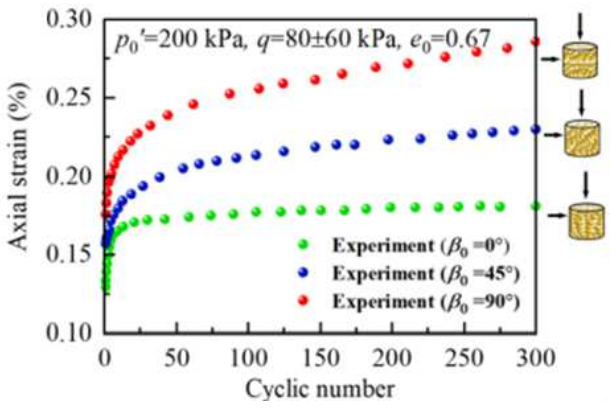

(a)

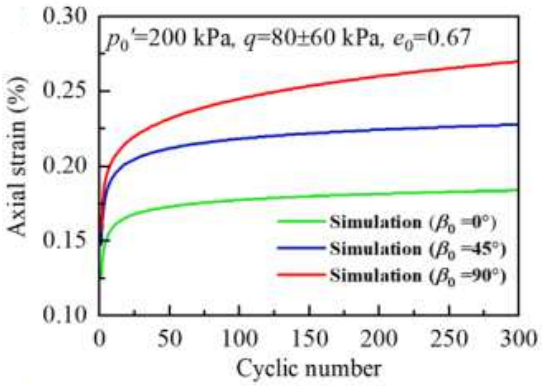

(b)

Figure 16. Influence of bedding plane angle β_0 on high-cycle axial strain accumulation: (a) experimental data, (b) simulated results

4 SOIL-PILE INTERACTION MODELS

4.1 Soil Flow Mechanism Around Monopiles

Monopile diameters (D) increased from the 4 – 6 m in the early stage to over 8 m currently and may reach 10 m in the future (Byrne et al., 2019). The embedded pile length to diameter ratio (L/D) of a monopile is typically within 4–8, but may reduce to 3 or lower in the future. Figure 17 presents the statistics of typical monopile geometries in China (Wang et al., 2021).

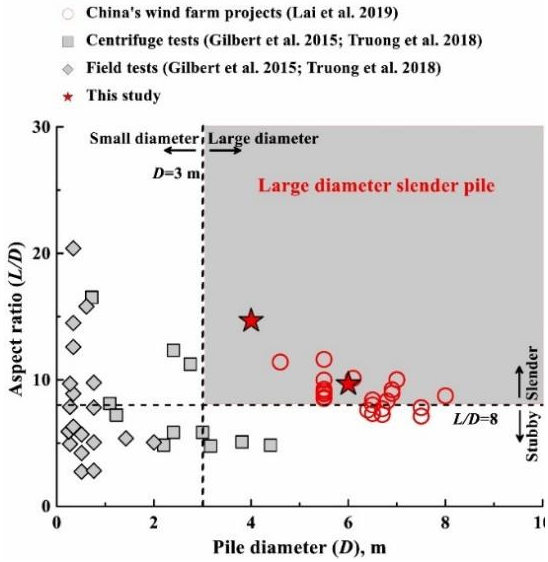

Figure 17. Statistics of monopile geometries (Wang et al., 2021

The design of laterally loaded monopiles is typically based on the *p-y* models (API, 2014; DNVGL, 2016), which were established according to field tests on long slender piles with D = 0.324 m and L/D = 39. Recent attempts to apply existing *p-y* models for monopile designs with larger D and smaller L/D were unsatisfactory, indicating these models cannot accurately capture the mechanical responses of large-diameter monopiles.

The authors' team has placed special emphasis on the soil failure mechanism around monopiles, which inherently links with the dependency of *p-y* on L/D.

Figure 18 illustrates the soil flow mechanism surrounding a semi-rigid pile embedded in soft clay, as observed within a 100g centrifuge environment (Hong et al., 2017). Meanwhile, Figure 19(a) presents a numerical simulation depicting the soil failure flow pattern for a semi-rigid pile (L/D = 8) in clay (Wang et al., 2020c), whereas Figure 19(b) shows a corresponding simulation for a rigid pile (L/D = 6) in sand (Wang et al., 2020c). Both centrifuge and numerical analyses have collectively demonstrated that the L/D ratio of a monopile, which is a dimensionless term governing the relative stiffness between the soil and the pile, plays an important role in determining its nearby soil flow mechanisms, and thus the modes of soil-pile interaction.

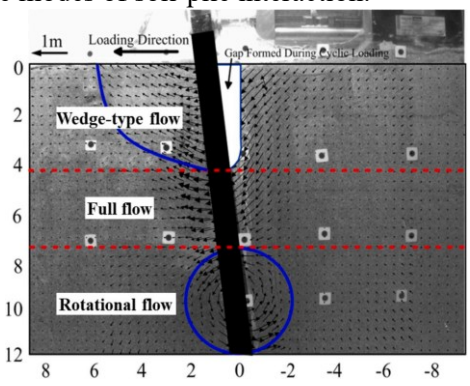

Figure 18. Measured soil flow mechanism around a semi-rigid pile in soft clay (Hong et al., 2017).

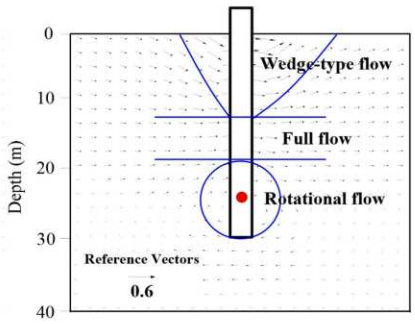

(a)

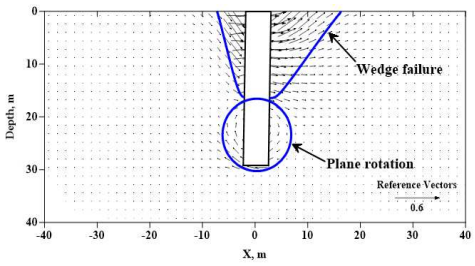

(b)

Figure 19. Soil flow mechanics around monopiles

4.2 "*p-y*+*M-θ*" Model for Monopile in Clay

Based on the merits and potential demerits of the existing models, Wang et al. (2020c) proposed a new two-spring model, i.e., "*p-y* + *M-θ*" model, as shown in Figure 20. It considers the three most important components resisting a laterally loaded monopile, namely (i) lateral soil resistance; (ii) base shear and (iii) base moment. Above the rotation point, the lateral soil resistance is modelled by distributed lateral translational springs (*p-y* springs), as routinely practiced. While the overall resistances at and below the rotation point, including the contributions from the rotational soil flow (as evident numerically and experimentally), base shear and base moment, are integrated into a concentrated rotational spring (*M-θ* spring) at the rotation point. The rotation point, which

involves a pure rotation with little lateral displacement, is usually located within a narrow range of depth z = (0.75–0.80) L. The well-defined boundary conditions and location of the rotation point bring convenience for constructing the "p-y + M-θ" model.

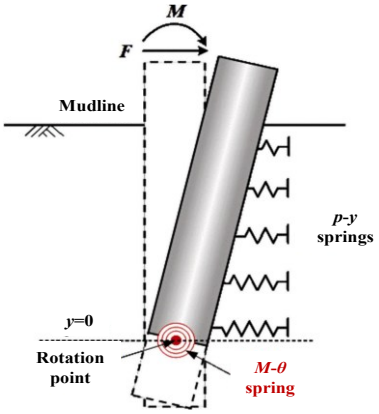

Figure 20. A new model proposed in this study for mono-piles with varied L/D.

Based on the Norwegian Geotechnical Institute (NGI) theoretical framework for cyclic contour lines, the stress-strain relationship for an equivalent number of cycles under simple shear can be scaled to derive p-y curves under cyclic loading. Recent advancements extend this to equivalent p-y curves for combined average and cyclic loading, as shown in Figure 21. Here, cyclic stress amplitude and mean stress are decoupled to obtain stress-strain curves for a specified equivalent number of cycles. These curves are scaled to separately compute monopile response under mean and cyclic loads, which are then superimposed. For this model, the cyclic contour line theory also applies to constructing cyclic M-θ curves. Using cyclic p-y and M-θ curves for equivalent cycles, the model can analyze monopile response under cyclic loading for varying pile stiffnesses, providing a versatile tool for practical engineering applications.

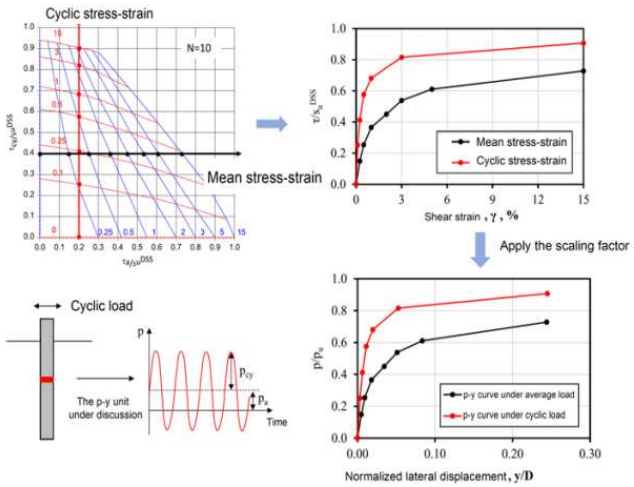

Figure 21. Deducing cyclic p-y curves from cyclic loading contour

4.3 Blind Prediction Competition in ISFOG-2020

During the 4th International Symposium on Frontiers in Offshore Geotechnics (ISFOG-2020), the University of Western Australia (UWA) organized a prediction competition for the monotonic and cyclic loading responses of laterally loaded piles in soft clay, using centrifuge model tests. Soil element test data were provided in advance for analysis. The author's team submitted predictions for both monotonic and cyclic loading responses based on the "p-y + M-θ" analysis model. Figure 22 illustrates elevation view of the model test in prototype scale. Table 2 summarizes all centrifuge tests, including one monotonic loading test and three bidirectional cyclic loading tests.

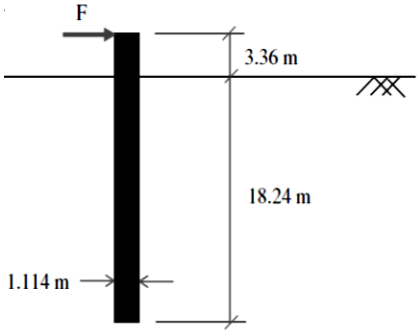

Figure 22. Elevation view of the model test in prototype scale

Table 2. Test program for the prediction event

Test	Test type	Amplitude		
		Displacement	Model scale	Prototype scale
Static loading（MT）	Monotonic loading	1.07D	14.90 mm	1.19 m
Cycle test 1（CT1）	Bidirectional displacement control	0.02 D	0.22 mm	0.02 m
Cycle test 2（CT2）	Bidirectional displacement control	0.10 D	1.37 mm	0.11 m
Cycle test 3（CT3）	Bidirectional Load Control	-	23.9 N	153 kN

Figure 23 shows the comparison between the meausred and predicted results for this contest. Specifically, Figure 23(a) presents the monotonic loading test results (black line) alongside all predicted load-displacement curves (gray lines), with the results from the "p-y + M-θ" model highlighted in red. Meanwhile, Figure 23(b) and (c) show the predicted and measured pile head responses and bending moment distributions along the pile at different cycle counts. Additionally, Figure 24 compares the predictive performance of all participants using the

peak bending moment along the pile as a benchmark. Notably, the "*p-y* + *M-θ*" model developed in this study accurately captures the monotonic and cyclic loading responses of monopiles, with its predictive accuracy ranking among the top of all participating models.

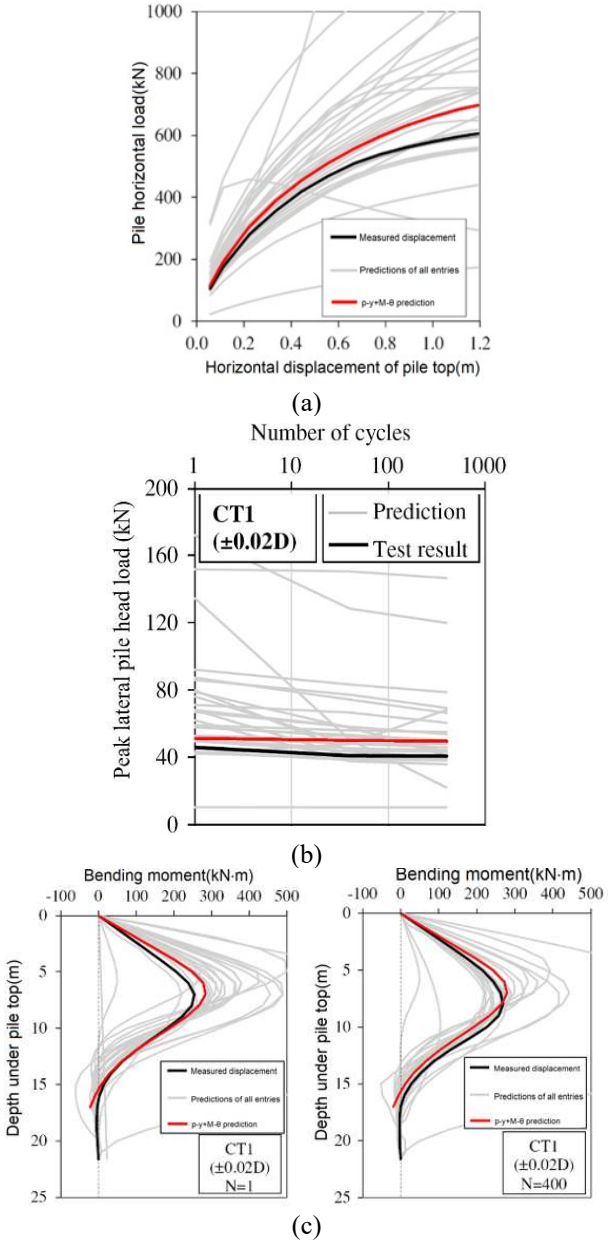

Figure 23. Cyclic loading prediction event (a) Monotonic lateral head load-displacement curves; (b) Pile head response against cycles number (N = 1, 40, and 400); (c) Bending moment profiles for N = 1 and 400 for each cyclic test

4.4 "*p-y+M-θ*" Model for Monopile in Sand

4.4.1 Sandy soil reaction model

Wang et al. (2023) presents a numerical investigation of the monotonic lateral response of large-diameter monopiles in drained sand with configurations typical of those employed to support offshore wind turbines. These analyses were then extended to examine the influence of pile diameter and loading eccentricity on the lateral response of rigid monopiles. The results show no dependency of suitably normalised lateral load transfer curves on the pile diameter and loading eccentricity. A normalisation method is subsequently proposed which unifies the load–deflection responses of rigid piles with different diameters at a given load eccentricity.

A soil reaction model for describing high-cycle behaviour of pile in sand is also develped using a series of non-linear springs. It incorporates a multi-yield surface kinematic hardening model (Houlsby et al., 2017; Zha et al., 2022) into the "*p-y+M-θ*" framework (Wang et al., 2020c). In the light of the soil flow mechanisms around monopiles, the lateral soil resistance within the upper half of the pile is described using a *p-y* model, while the resistances around the rotation point RP near the lower half of the pile are integrated into a moment-rotation spring (characterized by a *M-θ* model) at the RP. The rotation point, which involves a pure rotation with little lateral displacement, is usually located within a narrow range of depth z= (0.7–0.80) L (Figure 25(a)).

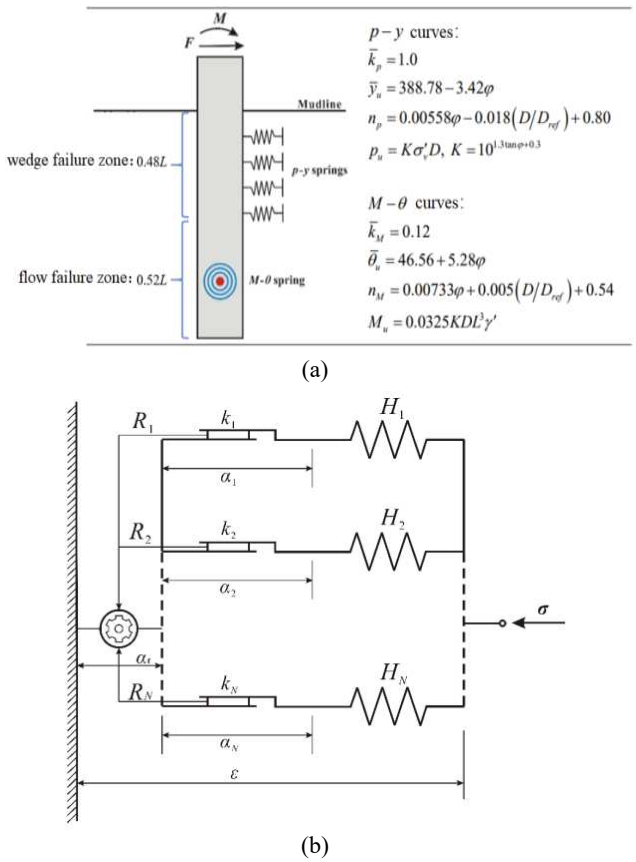

Figure 25. (a) The "p-y+ M-θ" model for monopile in sand; (b) Schematic diagram of the spring-slider-ratchet element assembly in the hyperplastic ratcheting model.

4.4.2 Accelerated ratcheting hyperplasticity

Houlsby et al. (2017) presents a well-designed model HARM for cyclic ratcheting analysis, as shown in Figure 25(b). The prediction accuracy of the multi-yield surface kinematic hardening model depends on the number of spring-slider units N and the distribution form of the initial backbone curve discrete points. To accurately simulate the nonlinear characteristics of the curve, the number of spring-slider units N is taken as 50 in the simulation. In the ratcheting model, the load characteristics and loading history effects are reflected through the definition of ratcheting coupling parameter expressions, as shown below (Beuckelaers, 2017):

$$R_i = R_0 \left(\frac{|\sigma|}{\sigma_u}\right)^{m_\sigma} \left(\frac{\sum y_i k_i}{\sigma_u}\right)^{m_k} \left(\frac{\alpha_h}{\alpha_{h0}}\right)^{m_h} \frac{k_i}{\sigma_u} \quad (15)$$

4.5 Blind Prediction Competition in ISFOG-2025

As an event of the 5th International Symposium on Offshore Geotechnical Engineering (ISFOG-2025) and part of the GEOLAB project, the Institute of Geotechnics of TU Darmstadt called industry and academia to participate in an international Blind Prediction Contest (BPC) on the response of piles under monotonic and cyclic lateral loading in 2024. Two separate tests were to be performed on a hollow open-ended steel pile embedded in dry sand. One test under monotonic loading and the other under quasi-static harmonic loading with more than 10,000 loading cycles. In this contest, a total of 18 teams submitted their predictions.

In the model test, the pile is assumed to be an Euler-Bernoulli beam, with the embedment depth L=2 m, the radius D=0.32 m, and the wall thickness t=0.00525 m, as shown in Figure 26.

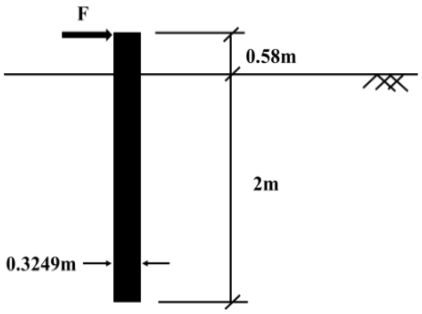

Figure 26. A schematic diagram showing test model pile

Four material constants are introduced in the ratcheting model, namely the initial hardening parameter α_{h0}, stress index m_σ, hardening index m_h and the ratcheting rate R_a. These four material constants for lateral loaded piles in sand have been carefully calibrated by Abadie et al. (2019), and are thus taken in this present analyses, as summarised in Table 3.

Table 3 List of material constants for the cyclic "p-y+M-θ" model.

Ratcheting parameters		Definition	Value	Reference
p-y	a_{ho}	initial hardening parameter	1×10^{-4}	Abadie (2019)
	m_σ	stress index	9.5	
	m_h	hardening index	-3.1	
	R_a	ratcheting rate	1.8	
M-θ	a_{ho}	initial hardening parameter	1×10^{-4}	Abadie (2019)
	m_σ	stress index	9.5	
	m_h	hardening index	-3.1	
	R_a	ratcheting rate	1.8	

The test was conducted in a geotechnical test chamber. Medium coarse sand was used in the model test. The sand was filled in layers and compacted, the averge relative density D_r=0.89.

To assess the compactness of sand at various depths and locations within the experimental container, seven standard Cone Penetration Tests (CPTs) were carried out following the initial compaction process, as illustrated in Figure 27(a). These tests utilized a conical probe with a base area of 10 cm² (designated as CPT 10). The penetration depth achieved was 2.5 meters. The cone resistance data obtained from these tests are illustrated in Figure 28(b).

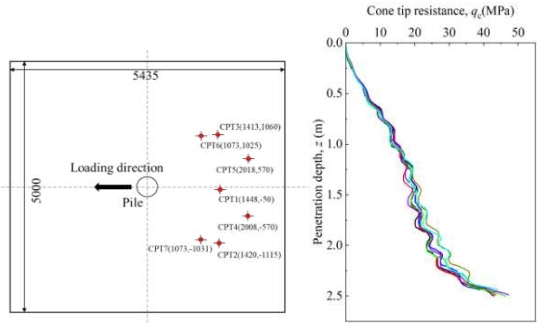

(a)Test arrangement (b) CPT results

Figure 27. Cone Penetration Test

Table 4 and Table 5 summarize the content of monotonic loading test and cyclic loading test respectively. In the monotonic test (MT), the loading rate of pile head is 1 mm/min. The cyclic test series consists of two experiments (CT1 and CT2), in which the cyclic loading frequency is 0.125Hz.

Table 4. Monotonic Loading Test

Stage	Loading mode	Description
MT	Displacement Control	Monotonic loading at 1 mm/min until reaching a displacement of the loading point of 65 mm with respect to the initial pile position.
	Force Control	Maintain the force achieved in Stage 1 constant for 20 minutes or until the displacement rate is lower than 0.02 mm/min, whichever occurs last.
	Displacement Control	Monotonic unloading at 1 mm/min until reaching a force $H = 0$

Table 5. Cyclic Loading Test

Stage	Loading mode	Description
CT 1	*Displacement Control*	*Monotonic loading at 1 mm/min until reaching a force* $H = H_{m1} = 0.2H_f$
	Force Control	*First cyclic loading package:* $H = H_{m1}+H_{c1}\sin(2\pi ft)$ *Mean force:* $H_{m1} = 0.2H_f$, *Amplitude:* $H_{c1} = 0.1H_f$ *Number of cycles:* $N = 10000$
	Displacement Control	*Monotonic unloading at 1 mm/min until reaching a force* $H = 0$
Stage	Loading mode	Description
CT 2	*Displacement Control*	*Monotonic loading at 1 mm/min until reaching a force* $H = H_{m2} = 0.5H_f$
	Force Control	*Second cyclic loading package:* $H = H_{m2}+H_{c2}\sin(2\pi ft)$ *Mean force:* $H_{m2} = 0.5H_f$, *Amplitude:* $H_{c2} = 0.2H_f$ *Number of cycles: continue cyclic loading until any of the following conditions is reached:* *1.* $N > 1000$ *and* $y_{max} > 33$*mm ;* *2.* $N > 3000$ *;* *3.* $y_{max} > 65$*mm*
	Displacement Control	*Monotonic unloading at 1 mm/min until reaching a force* $H = 0$

For the monotonic loading prediction of single pile, the parameter selection of "*p-y* + *M-θ*" backbone curve proposed was determined based on the CPT data. Considering that φ' varies with stress level, Bolton (1986) relates φ' to stress level and relative densities, as shown in Figure 28(a). In the case of D_r = 0.89, linear interpolation yields an internal friction angle φ' of 45°, which broadly represents the average friction angle deduced from CPT test (Figure 28(b)).

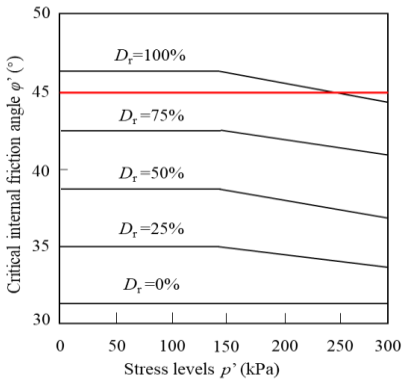

(a) Relationship between φ 'and stress level *p*' at different relative density D_r

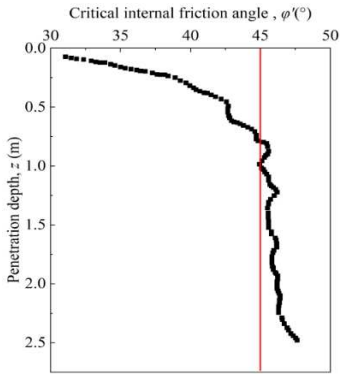

(b) Empirical formula to calculate values

Figure 28. The predicted model's internal friction angle

The normalized quantity G_0 is calculated by the formula proposed by Senetakis et al. (2013):

$$G_0 = Ae^x P_a(\sigma'_m/P_a)^n \qquad (15)$$

where e is the void ratio, σ'_m is the average effective stress, A=570.1-58.8C_u, x=-0.28C_u-0.98, n=0.47, C_u is the coefficient of inhomogeneity. The above parameters can be obtained according to the test data provided by the organizer.

All teams submitted a total of 25 sets of predictions, including 18 sets of predictions for monotonic loading and 7 sets of predictions for cyclic loading. Figure 29 shows the results of the monotonic loading test (in black line) and the predictions submitted by all teams (in gray line). Among these predictions, the predictions based on the "*p-y* + *M-θ*" model in this paper are shown in red lines. It demonstrates that when the horizontal pile displacement reaches 60mm at the loading point, the majority (89%) of predictions significantly underestimate the applied load. While the median prediction across all models is 32% lower than the measured data. The "*p-y* + *M-θ*" model shows reasonable accuracy with only 18% deviation from the measured value, ranking among the top-performing predictive methods in this comparative study. This consistent discrepancy likely originates from underestimated internal friction angles, particularly in 1g model tests conducted under low stress conditions where sand exhibits enhanced dilative behavior.

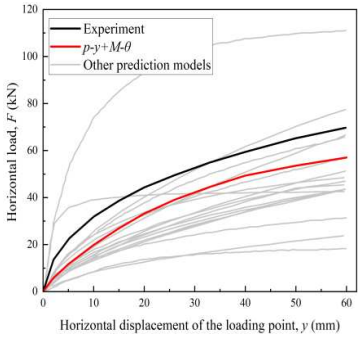

Figure 29 Monotonic lateral load-displacement curves

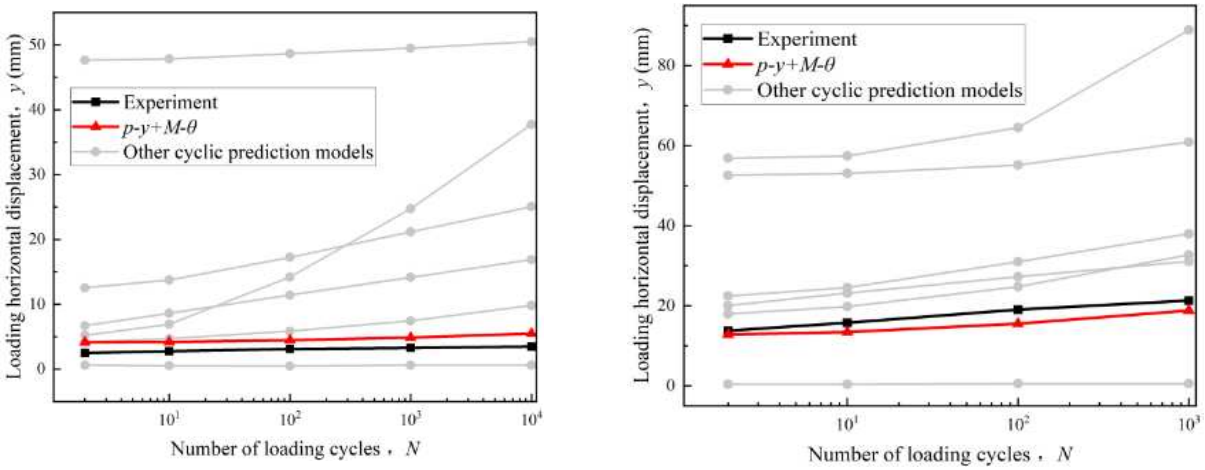

Figure 30. (a) The first cyclic loading package results; (b) The second cyclic loading package results.

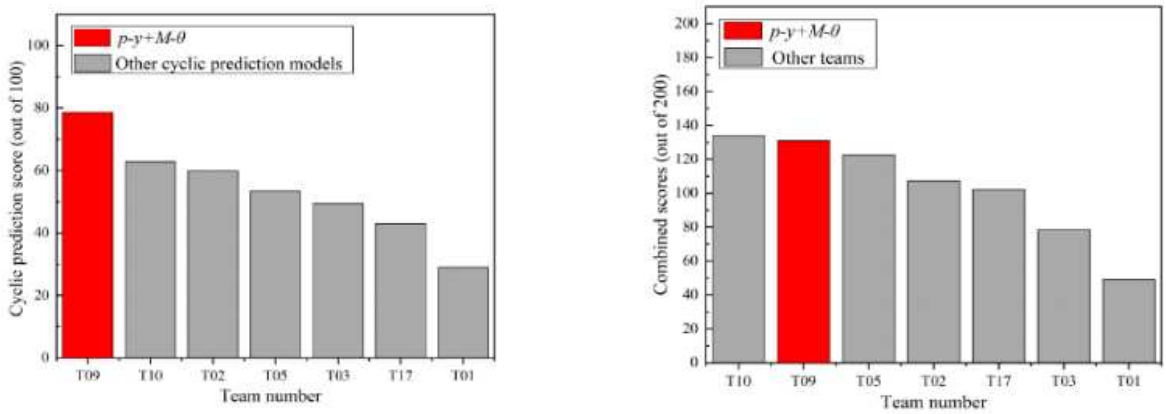

Figure 31. (a) Ranking for the cyclic test predictions; (b) Overall ranking for both cyclic and monotonic test predictions

The predictive performance of the proposed model for cyclic loading tests is illustrated in Figure 30, where it achieved the highest accuracy ranking among all evaluated models. It is the only model that manages to predict the shakedown response of the laterally loaded pile under a total of 13000 cycles. When considering the combined performance under both static and cyclic loading conditions (as summarized in Figure 31, the proposed model secured the second-place ranking overall. Notably, the "*p-y + M-θ*" model demonstrates superior predictive capabilities, particularly in capturing high-cycle lateral displacement accumulations.

5 MULTIBODY DYNAMICS AND SOFTWARE

5.1 Aero-hydro-seismic-servo Multi-body Dynamics

As a multi-body system, the response of offshore wind turbines can be determined using the Kane dynamic equations (Wang et al., 2024):

$$\sum_{r=1}^{R}(F_r + F_r^*) = 0 \tag{16}$$

where R represents the total number of degrees of freedom of the turbine system. F_r and F_r^* are the generalized main force and generalized inertial force in the r^{th} degree of freedom, which can be calculated as:

$$F_r = \sum_{n=1}^{N} v_r^{RP_n} \cdot F^{RP_n} + w_r^n \cdot M^n \tag{17}$$

$$F_r^* = \sum_{n=1}^{N} v_r^{RP_n} \cdot m^n \cdot \ddot{q}^{RP_n} + w_r^n \cdot H^n \tag{18}$$

All the terms above are computed in the inertial coordinate system, where N denotes the number of bodies in the structure, $v_r^{RP_n}$ and w_r^n represent the translational and rotational velocities, respectively, of body n at its dynamic reference point RP_n, and m^n is the mass of body n. H^n is the time derivative of the angular momentum of body n about its reference point. F^{RP_n} and M^n are the active force and active moment acting on the body n. By classifying and rearranging

the terms in Eq. (16) based on whether they contain $\ddot{q}$, the following equation can be obtained.

$$M(q,t)\ddot{q} = -f(\dot{q},q,t) \tag{19}$$

In this equation, $M(q,t)$ consists of the terms related to $\ddot{q}$ from the generalized active forces and generalized inertial forces, while $-f(\dot{q},q,t)$ represents the combination of terms independent of $\ddot{q}$. This system can be solved using Gaussian elimination, LU decomposition, or other methods, with various algorithms, i.e., the 4th-order Runge–Kutta method or the 4th order Adams-Bashforth-Moulton predictor-corrector method for time stepping.

Schematic diagram of Zwind 2.0 software is shown in Figure 32, with the following new and unique features:

- the environmental loading prediction is achieved including typhoon, typhoon wave and earthquake, i.e., maximum wind speed, wave period, wave height, and seismic accelerations, velocities and displacements along the pile elevation (Wang et al., 2025).
- As for monopile design, a series of advanced soil-structure interaction models are developed to tackle the deteriorated seabed condition, such as the widely-used API *p-y* model, the "*p-y+M-θ*" model (Wang et al., 2020c), the "*p-y+M-θ*" plus HARM model (Zha et al., 2022) and the multi-directional model based on bounding surface plasticity (Hong et al., 2023) and
- a couple of control algorithms are proposed for loading mitigation, known as active torque control (Wang et al., 2024); feedback-forward control (Chen et al., 2024).

5.2 Application of Zwind 2.0 for monopile design

The Taizhou No.1 wind farm, a total of 40 monopile wind turbines with 7.5MW in capacity stand in soft soil. The schematic of monopile offshore wind turbine is shown in in Figure 33, accompanied by the distribution of undrained shear strength along the monopile embedment. Properties of the DEW-D7500-204 OWT and monopile support structure are summarized in Table 6.

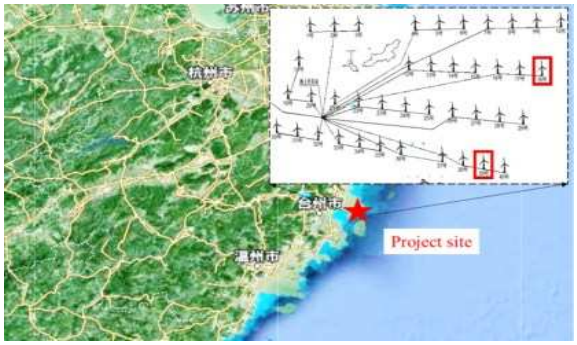

(a)

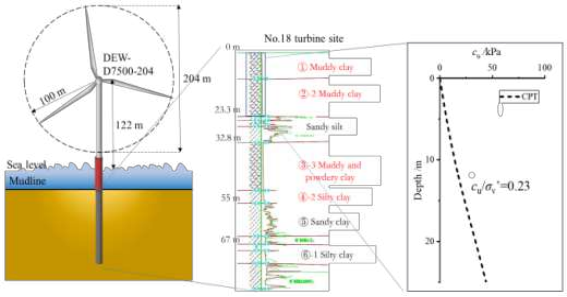

(b)

Figure 33. Characteristics of Taizhou No.1 wind farm

Table 6. Properties of the DEW-D7500-204 OWT with a monopile support structure

Rating	7.5MW
Rotor orientation, configuration	Upwind, 3 blades
Rotor diameter	203.3 m
Hub-height	121.2 m
Cut-in, rated, cut-out wind speed	3, 11, 25 m/s
Rated rotor speed	9.5 rpm
Rated tip speed	80 m/s
Rotor mass	172,107 kg
Nacelle mass	268,532 kg
Supporting structure mass	924,928 kg
Mean sea level	20.0m
Tower top diameter, wall thickness	3.87, 0.019 m
Tower base diameter, wall thickness	6.0, 0.027 m
Substructure diameter, wall thickness	6.0, 0.06 m

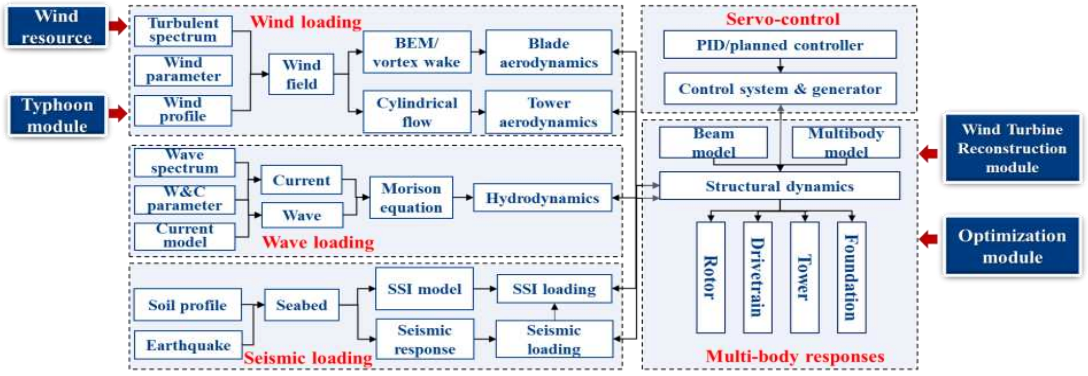

Figure 32. Schematic diagram of Zwind software

Integrated dynamic analyses and fatigue life prediction of the Taizhou No.1 wind turbine are conducted with Zwind software considering the load cases as summarized in Table 7. Each simulation lasts for 700 s (with the first 100s responses removed) and results of 10 seeds are averaged to predict fatigue damage. The rain-flow counting method is adopted to evaluate damages of wind turbine monopiles. As a typical response, the bending moment time histories at the mudline are compared in Figure 34. It can be seen that the bending moment extracted from the idling/parked condition shows a smaller maximum value, but more fluctuations compared to that in the normal operation. All blades are pitch-featured in the parked/idling condition, leading to the loss of aerodynamic load and magnifying hydrodynamic load due to the factor that aerodynamic damping vanished under the idling condition (Valamanesh and Myers, 2014).

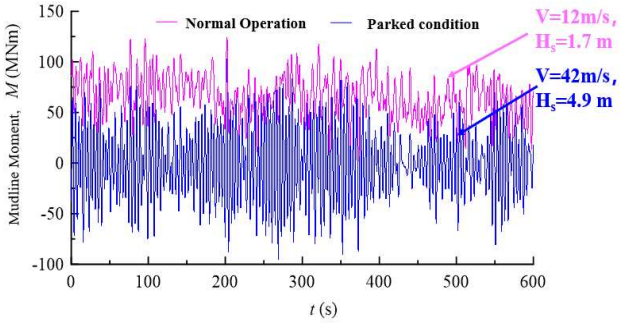

Figure 34. Variation of bending moment with time at mud-line against operational scenario

The annual fatigue damage and its corresponding fatigue life are compared to demonstrate the influence of SSI model in Figure 35. It is found that the "*p-y+M-θ*" model would yield a safer and more economic monopile scheme than the widely-used API *p-y* model as the longer fatigue life is predicted, which leads to a reduction of 5 m in monopile length at No.18 and No.39 wind turbines at the Taizhou No.1 wind farm. It also means much cost can be saved if all wind turbines are designed using the "*p-y+M-θ*" model instead of the API *p-y* model.

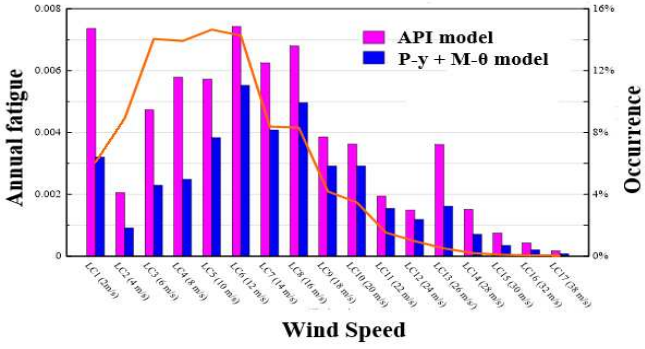

(a)

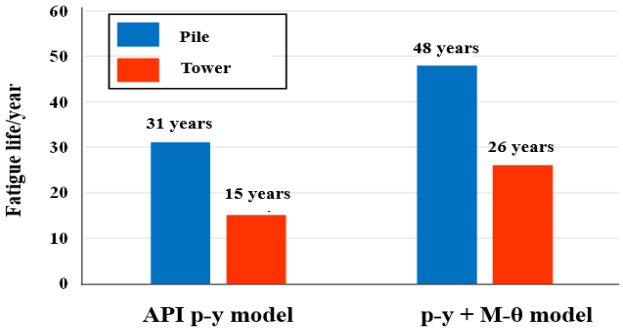

(b)

Figure 35. Fatigue damage prediction: (a) annual fatigue at different wind speeds; (b) fatigue life predicted based on different soil-pile interaction model

Table 7. Load cases for fatigue analysis

Load case	Wind speed V (m/s)	Wave height Hs (m)	Wave period Tp (s)	Probability f (%)	Operational scenario
LC1	2	1.07	6.03	6.071	Parked
LC2	4	1.1	5.88	8.911	
LC3	6	1.18	5.76	14.048	
LC4	8	1.31	5.67	13.923	
LC5	10	1.48	5.74	14.654	
LC6	12	1.70	5.88	14.272	
LC7	14	1.91	6.07	8.381	Normal operation
LC8	16	2.19	6.37	8.316	
LC9	18	2.47	6.71	4.186	
LC10	20	2.76	6.99	3.480	
LC11	22	3.09	7.40	1.534	
LC12	24	3.42	7.80	0.974	
LC13	26	3.76	8.14	0.510	
LC14	28	4.17	8.49	0.202	
LC15	30	4.46	8.86	0.096	Parked
LC16	32	4.79	9.12	0.050	
LC17	42	4.90	9.43	0.019	

6 NOVEL TECHNIQUE FOR MONOPILE INSTALLATION

6.1 Transition-piece-free Monopile

During the early phase of offshore wind farm developments in Europe, limitations in construction equipment and techniques made it difficult to control the verticality of monopiles. As a result, monopile with transition piece (Figure 36(a)) has been predominantly adopted, where the transition piece was used to adjust the verticality after the monopile was driven into the seabed, ensuring compliance with the installation requirements for wind turbines (≤0.25°, approximately 4.3‰). Given the wide application of the monopile with transition piece, several serious issues emerged in the wind turbines structure after several years of service. At the "China-UK Offshore Wind Case Study

Conference" organized by the National Energy Administration on March 18, 2014, UK offshore wind experts reported that more than 600 out of over 900 transition piece monopiles in the UK had experienced turbine tilting accidents due to fatigue failure of the grouting at the transition piece. Despite the significant time and effects invested, the risk of fatigue failure at the transition piece remains. At the same conference, the authors' team (i.e., Jiangsu Longyuan Zhenhua Marine Engineering Co., Ltd.) reported and demonstrated China's successful development of transition-piece-free monopile (Figure 36(b)), marking a significant advancement in offshore wind foundation technology in China.

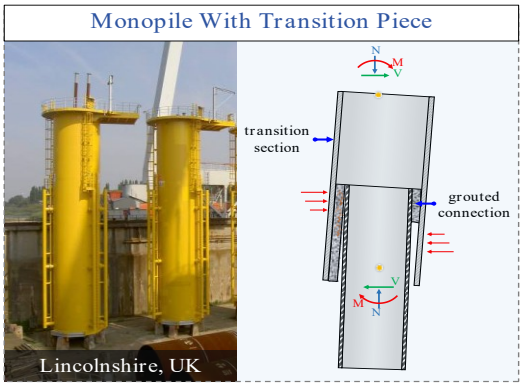

(a)

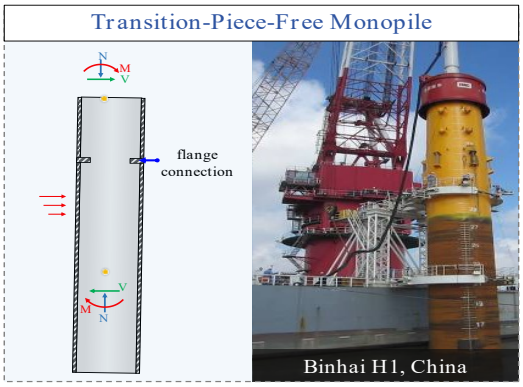

(b)

Figure 36. (a) Monopile with transition piece, (b)transition-piece-free monopile

6.2 Equipment for controlling pile verticality

The transition-piece-free monopile foundation offers lower costs and much higher installation efficiency. This design was indeed initially applied in European offshore wind farms, such as the Scroby Sands Offshore Wind Farm in the UK in 2004, where 30 Vestas V80-2.0MW turbines were installed using transition-piece-free monopile foundations. However, due to immature construction equipment and techniques at the time, it was challenging to control the verticality of the monopiles. As a result, transition-piece-free monopile foundations were not used in European offshore wind farms for nearly a decade following this project.

To address the challenge of controlling the verticality of large-diameter, transition-piece-free monopiles in deep soft soil, a double-layer hydraulic monopile gripper with internal 100-ton servo-controlled hydraulic actuators for tilting correction was developed (Figure 37).

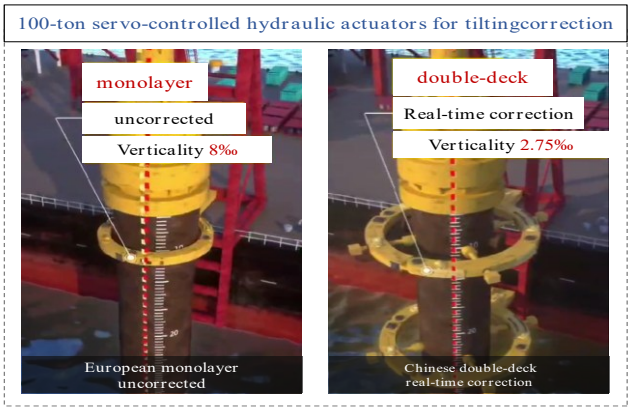

Figure 37. Double-layer servo-controlled hydraulic monopile gripper

This equipment was first applied in the 2011 Longyuan Rudong Intertidal 150 MW Demonstration Wind Farm in Jiangsu, China, achieving verticality control within 3‰ for 17 transition-piece-free monopile foundations. Subsequently, this technology was widely adopted in China's offshore wind projects, reducing the verticality deviation from the previous exercise of 8‰ to 2.75‰ and improving construction efficiency from the traditional 3 days per turbine to 1 day per turbine. This advancement has significantly promoted the application of transition-piece-free monopile foundations in China's offshore wind projects, accounting for approximately 70% of installations.

The successful application of transition-piece-free monopile foundations in China has also influenced the European offshore wind market in recent years. For example, between 2014 and 2015, the Netherlands adopted this technology in two offshore wind farms: the Eneco Luchterduinen Offshore Wind Farm, which installed 43 transition-piece-free monopile foundations for 3 MW turbines at water depths of 18–22 meters, and the Westermeerwind Offshore Wind Farm, which installed 48 transition-piece-free monopile foundations for 3 MW turbines at water depths of 3–7 meters.

7 CONCLUDING REMARKS

This keynote paper has reported recent contributions made by the authors' interdisciplinary team towards

resolving the challenges facing OWT foundation design and installation under such severe natural conditions in China. These advanced foundation design and installation technologies have been applied to 76 wind farms across China's four major sea areas, contributing to an installed capacity of 18.3 GW (approximately 60% of the national total), with the supported offshore wind turbines safely enduring over a hundred typhoons. Building on these advancements, the paper is structured into five parts, each targeting a critical aspect relevant to OWT foundation design and installation.

Part I focuses on modelling of extreme sea state under typhoon. The full typhoon track, zonation of typhoon wind speeds, in the Southeastern coastal area of China are obtained based on advanced numerical modelling supplemented with long-term field measurements. Part II reports behavior modelling of marine soils. The in-situ behavior of marine soil, including anisotropy, cyclic accumulation, rate- and temperature-dependency, are described in a unified way through new constitutive laws. Part III presents research supporting safe yet economical design of OWTs foundations in typhoon-prone area with soft soil. Part IV reports the implementation of these SSI models in the rigid–flexible multibody dynamics framework, enabling the development of Zwind software that renders coupled nonlinear aero-hydro-servo-elastic simulation of OWTS. Part V outlines novel techniques which greatly improve feasibility of monopile installation in very soft seabed.

As the development of nearshore wind farms nears completion, the focus is shifting to deep-water offshore wind energy. However, the high costs associated with deep-water projects remain a significant barrier. Revolutionary innovations in foundation types, such as hybrid fixed-floating turbines that cancel reliance on mooring systems, may provide a viable pathway to overcoming these challenges. Interdisciplinary efforts in this regard can significantly enhance the efficiency of deep-water wind energy development.

AUTHOR CONTRIBUTION STATEMENT

L. Z. Wang: Data curation, Formal analysis, Writing-Original draft, Writing-review & editing, Supervision, Funding acquisition. **Y. Hong, Z. Guo, Y. Y. Gao, M. F. Huang, L. L. Wang, H. Y. Jiang, R. Liu**: Data curation, Formal analysis, Writing- Original draft. **B. He, Y. F. Lin, G. K. Yuan, X. X. Feng**: Project administration, Resources. **S.G. Wu, P. Yin**: Data curation, Formal analysis.

ACKNOWLEDGEMENTS

The authors gratefully acknowledge the financial supports from the National Key R&D Program of China (2023YFB4203300), and National Natural Science Foundation of China (52238001, U24B20113 and 51939010).

REFERENCES

Abadie, C.N., Houlsby, G., Byrne, B. (2019) A method for calibration of the hyperplastic accelerated ratcheting model, *Computers and Geotechnics*, 112, pp. 370-385.

API (2014) Recommended practice planning, designing, and constructing fixed offshore platforms-working stress design, API 2A-WSD, API, Washington, DC.

Asaoka, A., Noda, T., Yamada, E., Kaneda, K., Nakano, M. (2002) An elasto-plastic description of two distinct volume change mechanisms of soils, *Soils and Foundations*, 42(5), pp. 47-57.

Beuckelaers, W. (2017) *Numerical modelling of laterally loaded piles for offshore wind turbines*, PhD thesis, University of Oxford.

Breiman, L. (2001) *Random Forests, Machine Learning*, 45(1), pp. 5-32. https://doi.org/10.1023/A:1010933404324.

Byrne, B.W., Burd, H.J., Zdravković, L., McAdam, R.A., Taborda, D.M.G., Houlsby, G.T., Jardine, R.J., Martin, C.M., Potts, D.M., Gavin, K.G. (2019) PISA: New design methods for offshore wind turbine monopiles, *Revue Française de Géotechnique*, 158, https://doi.org/10.1051/geotech/2019009.

Camargo, S.J., Robertson, A.W., Gaffney, S.J., Smyth, P., Ghil, M. (2007) Cluster analysis of typhoon tracks. Part I: General properties, *Journal of Climate*, 20(14), pp. 3635-3653, https://doi.org/10.1175/JCLI4188.1.

Chen, Z.G., Wang, L.L., Wang, L.Z., Hong, Y., Zhang, B.F., Yang, Q.M. (2024) Integrated analysis of hybrid control for offshore wind turbines: A case study in wave resonance prone wind farms, *Ocean Engineering*, 298, 117176.

Dafalias, Y.F. (1986) Bounding surface plasticity. I: Mathematical foundation and hypoplasticity, *Journal of Engineering Mechanics*, 112(9), pp. 966-987, https://doi.org/10.1061/(ASCE)0733-9399(1986)112:9(966).

DNV GL (2016) Design of Offshore Wind Turbine Structures (DNV-OS-J101), DNV GL, Oslo, Norway.

DNV GL (2016) DNVGL-ST-0126: Support Structure for Wind Turbines, DNV GL, Oslo, Norway.

DNV (2021) DNV-ST-0126: Support Structure for Wind Turbines, DNV GL, Oslo, Norway.

EWEA (2016) The European Offshore Wind Industry: Key Trends and Statistics 2017, Vol. 33.

Hong, Y., He, B., Wang, L.Z., Wang, Z., Ng, C.W.W., Mašín, D. (2017) Cyclic lateral response and failure mechanisms of a semi-rigid pile in soft clay: Centrifuge tests and numerical modeling, *Canadian Geotechnical Journal*, 54, pp. 806-824.

Hong, Y., Yao, M.H., Wang, L.Z. (2023) A multi-axial bounding surface py model with application in analyzing pile responses under multi-directional lateral cycling, *Computers and Geotechnics*, 157, 105301.

Hong, Y., Wang, X., Wang, L. (2024) High-cycle shakedown, ratcheting and liquefaction behavior of anisotropic granular material with fabric evolution: Experiments and constitutive modelling, *Journal of the Mechanics and Physics of Solids*, 187, 105638.

Houlsby, G.T., Abadie, C.N., Beuckelaers, W.J., Byrne, B.W. (2017) A model for nonlinear hysteretic and ratcheting behaviour, *International Journal of Solids and Structures*, 120, pp. 67-80.

Huang, M., Wang, Q., Jing, R., Lou, W., Hong, Y., Wang, L. (2022a) Tropical cyclone full track simulation in the western North Pacific based on random forests, *Journal of Wind Engineering and Industrial Aerodynamics*, 228, 105119, https://doi.org/10.1016/j.jweia.2022.105119.

Huang, M., Wang, Q., Liu, M., Lin, N., Wang, Y., Jing, R., Sun, J., Murakami, H., Lou, W. (2022b) Increasing typhoon impact and economic losses due to anthropogenic warming in Southeast China, *Scientific Reports*, 12(1), 14048, https://doi.org/10.1038/s41598-022-17323-8.

International Electrotechnical Commission (2009) Wind energy generation systems – Part 1: Design requirements, IEC 61400-1, IEC, Geneva.

Ishihara, K., Towhata, I. (1983) Sand response to cyclic rotation of principal stress directions as induced by wave loads, *Soils and Foundations*, 23(4), pp. 11-26.

Leroueil, S. (1997) Critical state soil mechanics and the behaviour of real soils, Recent Developments in Soil and Pavement Mechanics, Rotterdam, Almeida, pp. 41-80.

Leroueil, S. (2001) Natural slopes and cuts: movement and failure mechanisms, *Geotechnique*, 51(3), pp. 197-243.

Leroueil, S., Marques, M.E.S. (1996) Importance of strain rate and temperature effects in geotechnical engineering, Measuring and Modeling Time Dependent Soil Behavior, *Geotechnical Special Publication* No. 61, ASCE, New York, USA, pp. 1-60.

Li, L.L., Dan, H.B., Wang, L.Z. (2011) Undrained behavior of natural marine clay under cyclic loading, *Ocean Engineering*, 38(16), pp. 1792-1805, https://doi.org/10.1016/j.oceaneng.2011.09.004.

Li, X.S., Dafalias, Y.F. (2012) Anisotropic critical state theory: Role of fabric, *Journal of Engineering Mechanics*, 138(3), pp. 263-275.

Liu, H.Y., Abell, J.A., Diambra, A., Pisano, F. (2019) Modelling the cyclic ratcheting of sands through memory-enhanced bounding surface plasticity, *Géotechnique*, 69(9), pp. 783-800.

Mei, W., Xie, S.P. (2016) Intensification of landfalling typhoons over the Northwest Pacific since the late 1970s, *Nature Geoscience*, 9(10), pp. 753-757, https://doi.org/10.1038/ngeo2792.

Papadimitriou, A.G., Chaloulos, Y.K., Dafalias, Y.F. (2019) A fabric-based sand plasticity model with reversal surfaces within anisotropic critical state theory, *Acta Geotechnica*, 14(2), pp. 253-277.

Qin, X.W., Shi, X.Y., Zhang, Y., Li, X.J., Li, J., Xiao, G.Y., Xu, Z.Q., Wang, H.B., Lu, W.C., Wu, H., Yao, Y.J., Shang, L.N., Yang, C.P., Wang, Z.B., Gao, H.F., Wang, M.J., Mi, B.B., Zhong, H.X., Hu, G., Chen, H.J., Huang, L., Luo, W.D., Mei, X., Xu, Z.Y., Tian, Z.X., and Wang, Z.L. (2020) Main achievements and understanding of 1∶1 million regional geological survey of China Seas, *Geology in China*, 47(5), pp. 1355-1369 (in Chinese).

Valamanesh, V., Myers, A.T. (2014) Aerodynamic damping and seismic response of horizontal axis wind turbine towers, *Journal of Structural Engineering*, 140(11), 04014090.

Wang, H., Wang, .Z., Hong, Y., He, B., Zhu R. H. (2020a). Quantifying the influence of pile diameter on the load transfer curves of laterally loaded monopile in sand. *Applied Ocean Research*, 101: 102196.

Wang, H. , Wang, L.Z., Hong Y., Maˇsín, D., Li, W., He, B., Pan, H. L. (2021). Centrifuge testing on monotonic and cyclic lateral behavior of large-diameter slender piles in sand. *Ocean Engineering* 226,108299

Wang, H., Bransby, M. F., Lehane, B. M., Wang, L. Z. and Hong, Y. (2023). Numerical investigation of the monotonic drained lateral behaviour of large-diameter rigid piles in medium-dense uniform sand. *Géotechnique* 73, No. 8, 689–700

Wang, K., Wang, L., Hong, Y. (2020b) Modelling thermo-elastic–viscoplastic behaviour of marine clay, *Acta Geotechnica*, 15(9), pp. 2415-2431, https://doi.org/10.1007/s11440-020-00917-9.

Wang, L.L., Ishihara, T. (2022) A semi-analytical one-dimensional model for offshore pile foundations considering effects of pile diameter and aspect ratio,

Ocean Engineering, 250, 110874, https://doi.org/10.1016/j.oceaneng.2022.110874.

Wang, L.L., Wang L.Z., Hong Y. (2024). Mitigation of side-to-side vibration of a 10MW monopile offshore wind turbine under misaligned wind and wave conditions by an active torque control. *Journal of Sound and Vibration*, 574, 118225.

Wang, L.L., Wang, S.Y., Wang, L.Z., Hong, Y. (2025) A dynamic py+ M-θ model for monopile in soft clay considering failure mechanism under combined actions of wind and earthquake, *Computers and Geotechnics*, 180, 107074.

Wang, L.Z., and Shen K. L. (2008). Rotational hardening law of K0 consolidated structured soft clays. *Chinese Journal of Geotechnical Engineering*, (6):863–72.

Wang, L.Z., Dan, H.B., Li, L.L. (2012) Modeling strain-rate dependent behavior of K0-consolidated soft clays, *Journal of Engineering Mechanics*, 138(7), pp. 738-748,

Wang, L.Z., Lai, Y.Q., Hong, Y., Mašín, D. (2020c) A unified lateral soil reaction model for monopiles in soft clay considering various length-to-diameter (L/D) ratios, *Ocean Engineering*, 212, 107492.

Wang, L.Z., Shen K. L., Ye S.H. (2008). Undrained shear strength of K0 consolidated soft soils. *International Journal of Geomechanics*, ASCE, 8(2): 105-113.

Wang, L.Z., Teng, L., Wang, L.L., Hong, Y., Guo, Z., Li, L.L. (2024) Foundation Configuration and Multi-Body Dynamics Modeling of the Wind Turbine and Foundation System, *Engineering Mechanics (in Chinese)*.

Wang, L.Z., Wang, K.J., Hong, Y. (2016) Modeling temperature-dependent behavior of soft clay, *Journal of Engineering Mechanics*, 172(8), 07016057.

Wheeler, S.J., Näätänen, A., Karstunen, M., Lojander, M. (2003) An anisotropic elastoplastic model for soft clays, *Canadian Geotechnical Journal*, 40(2), pp. 403-418.

Wichtmann, T. (2005) *Explicit Accumulation Model for Non-Cohesive Soils Under Cyclic Loading*, PhD thesis, Bochum University, Bochum, Germany.

Yang, M., Taiebat, M., Dafalias, Y.F. (2022) SANISAND-MSf: A sand plasticity model with memory surface and semifluidised state, *Géotechnique*, 72(3), pp. 227-246, https://doi.org/10.1680/jgeot.19.P.363.

Zha, X., Guo, Z., Wang, L., Rui, S. (2022) A simplified model for predicting the accumulated displacement of monopile under horizontal cyclic loadings, *Applied Ocean Research*, 129, 103389.

Zheng, S.Y., Wang, L.L., Wang, L.Z., Wu, L.J., Hong, Y. (2024) Multi-objective performance enhancement of offshore wind turbines through planning controller parameter: A 'Plan-Control' hierarchical controller, *IEEE Transactions on Sustainable Energy*.

Zhu, J., Gao, Y., Wang, L., Li, W. (2022) Experimental investigation of breaking regular and irregular waves slamming on an offshore monopile wind turbine, *Marine Structures*, 86, 103270.